

## The Vertical Structure of Low-Frequency Motions in the Nearshore. Part I: Observations

THOMAS C. LIPPMANN

*Department of Earth Sciences, Center for Coastal and Ocean Mapping, University of New Hampshire,  
Durham, New Hampshire*

EDWARD B. THORNTON AND TIMOTHY P. STANTON

*Department of Oceanography, Naval Postgraduate School, Monterey, California*

(Manuscript received 14 January 2016, in final form 21 September 2016)

### ABSTRACT

Field observations of oscillating currents in the surfzone of a natural beach show significant vertical structure in energy, phase, and rotation at low frequencies around 0.005 Hz, where most of the energy is associated with vorticity motions. Energy levels in the cross-shore component of the flow seaward of the sandbar decay near the bottom. Shoreward of the bar crest, the flow decays nearly linearly over the water column. Conversely, a weaker alongshore component of the flow increases near the bottom seaward of the sandbar and is roughly depth-uniform inside the bar crest. Near this 0.005-Hz frequency band, the coherence between the uppermost and successive vertically separated sensors drops off quickly, with as much as a 70%–80% coherence drop over the water column (ranging from 2.5 to 4 m). The phase relative to the uppermost sensor shifts approximately linearly over depth, with as much as 50° phase lag at the bottom that can lag or lead the surface. Rotary coefficients also vary across the surfzone and are generally nonzero with rotational directions (cyclonic or anticyclonic) and orientation that depend on sensor position relative to the sandbar and alongshore current profile. The rotary coefficients are generally not uniform with depth and can change sign in the vertical. The observed behavior is qualitatively predicted by boundary layer theory (discussed in the companion paper by Lippmann and Bowen). The nonuniform vertical structure has implications to the interpretation of field data and horizontal nearshore mixing.

### 1. Introduction

Nearshore dynamics on natural beaches are based on complex interactions between surface waves and topography through nonlinear wave–wave and wave–bottom interactions that include turbulence and dissipation processes. These interactions produce three-dimensional circulation that is composed of both mean flows and oscillating motions at a variety of temporal scales. Nearshore flow has a horizontal variation that depends on alongshore changes in the wave field and topographical irregularities, and it has a variation with depth that arises from a vertical distribution of momentum flux induced by surface wave breaking and bottom friction. The focus here is on the vertical distribution of very low-frequency motions (with frequencies

around 0.005 Hz; 200-s oscillations), but for convenience of discussion, the flow is partitioned into temporal scales corresponding to mean flow, infragravity ( $<0.05$  Hz), and seaswell ( $>0.05$  Hz) frequency bands.

Considerable effort has been expended in measuring and modeling the vertical variation of mean flow patterns in and near the surfzone. In general, mean cross-shore currents are characterized by an undertow profile (Svendsen 1984; Haines and Sallenger 1994; Garcez Faria et al. 2000), whereas mean alongshore currents have an approximately logarithmic boundary layer spanning the water column (Visser 1986; Simons et al. 1992; Garcez Faria et al. 1998; Reniers et al. 2004b). In the surfzone, temporal variations in mean flow patterns occur on time scales associated with tides (Thornton and Kim 1993), changes in the wave forcing (Reniers et al. 2004a; MacMahan et al. 2004a), and through nonlocal circulation induced by bathymetric irregularities (Putrevu et al. 1995; MacMahan et al. 2004b).

---

*Corresponding author address:* Thomas C. Lippmann, University of New Hampshire, 24 Colovos Rd., Durham, NH 03824.  
E-mail: lippmann@ccom.unh.edu

Oscillating flow patterns with periods of 20–200 s (infragravity waves) are associated with either forced motions linked to the wave groups (e.g., [Guza and Thornton 1985](#); [Elgar and Guza 1985](#)) or free-surface gravity waves (edge and leaky waves; e.g., [Eckart 1951](#); [Bowen and Guza 1978](#)). At time scales of 200 s and greater, motions are a combination of infragravity waves and a variety of vorticity motions, including shear instabilities of the alongshore current (so-called shear waves; [Bowen and Holman 1989](#); [Oltman-Shay et al. 1989](#); [Dodd and Thornton 1990](#)), oscillatory motions arising from direct forcing by wave groups ([Long and Özkan-Haller 2009](#)), unforced motions associated with rip current cells ([Geiman and Kirby 2013](#)), and variations in surfzone breaking patterns of individual waves ([MacMahan et al. 2010](#); [Clark et al. 2012](#); [Feddersen 2014](#)). The energy of these oscillations was shown in frequency–wavenumber spectra to be outside the range of surface gravity wave motions (zero-mode edge waves). Vorticity motions differ from infragravity waves in that they are primarily horizontal motions, and gravity is not their restoring force. Some vertical motions (shear waves) only exist in the presence of strongly sheared currents (alongshore current in this case) with an inflection point in the background vorticity field ([Howd et al. 1991](#); [Lippmann et al. 1999](#); [Noyes et al. 2004](#)).

Although it long has been observed that the mean flow field has significant vertical variation, ranging from parabolic (e.g., undertow in the cross shore) to logarithmic (e.g., mean alongshore current) profiles, the majority of the literature examining infragravity waves and vorticity motions assumes that the flow field is uniform with depth. Much of the theoretical behavior of both infragravity waves and other vortical motions with small-amplitude surface elevations (e.g., shear instabilities of the longshore current) can be verified by observing the spatial scales of the motions ([Oltman-Shay et al. 1989](#); [Noyes et al. 2004](#)) or via an integrated spectral approach that lumps all the infragravity wave modes together to see how the overall energy varies with conditions and across the beach profile ([Lippmann et al. 1999](#)). As a consequence, it has long been assumed that the essential dynamics of these low-frequency motions can be measured from a single sensor located at some arbitrary elevation above (but usually close to) the bottom or with a horizontally spaced alongshore array whereby each sensor is located at, perhaps, a different elevation.

[Zhao et al. \(2003\)](#) use the quasi-3D model ShoreCirc ([Van Dongeren and Svendsen 2000](#); [Svendsen et al. 2002](#)) to model nearshore circulation and examine the spatial structure of shear instability motions. In ShoreCirc, the horizontal, depth-averaged variation in shear instability

energies are modeled and then the vertical structure is applied through a spatially varying dispersion term that arises from depth integrating local, depth-varying currents (following [Putrevu and Svendsen 1995](#)). [Zhao et al.](#) show that instantaneous velocity profiles for shear instabilities can vary over the vertical with sometimes higher velocities at the bed and with flows at the surface that are in opposite direction than near the bottom. Their simulations suggest that three-dimensional effects in shear instabilities are possible and result from dispersive mixing mechanisms.

In this work, we discuss observations that reveal a complex vertical structure in low-frequency motions. As the dynamics of surface gravity waves and vorticity motions are much different, we will restrict our discussions to a very low-frequency band at  $f = 0.005$  Hz, where nearly all the motions are associated with vorticity dynamics. In the following, we first discuss the field measurements and then present observations that show significant vertical structure in energy levels, phase relationships, and rotational components of the low-frequency flow field. The observations show that vorticity motions are significantly more complex than previously believed. Implications of the observed behavior for the interpretation of field data and nearshore mixing are discussed.

## 2. Field measurements

Field measurements were acquired as part of the comprehensive Duck94 nearshore processes experiment held at the U. S. Army Corps of Engineers Field Research Facility (FRF), in Duck, North Carolina, during the fall of 1994. A detailed description of the field site can be found in [Lippmann et al. \(1993\)](#), and a more complete description of Duck94 and the instrumentation used in this study can be found in [Garcez Faria et al. \(1998, 2000\)](#), [Feddersen et al. \(1996, 1998\)](#), and [Gallagher et al. \(1998\)](#). Observations are available online ([Thornton and Stanton 1994](#)). In the following, we summarize the important information for completeness.

The FRF is located on a long, nearly straight section of the Outer Banks (a barrier island formation), well away from inlets. The intertidal beach slope is about 1:12 and flattens to about 1:170 outside the surfzone. There is usually a prominent, mobile sandbar within about 50–150 m of the shore and a lower-amplitude, more seaward second bar within about 400 m of the shore that has lower mobility and is not always present. The mean (semidiurnal) tide range is about 1 m. Sediments within the surfzone are well sorted with a mean grain size of 0.2 mm, and in the intertidal region grains are larger (mean size >0.4 mm) and poorly sorted.

The data utilized in this study were obtained on 10–12 October, a period when strong alongshore currents (peaking at about  $1 \text{ m s}^{-1}$ ; Garcez Faria et al. 1998) and undertow (with subsurface maxima of about  $0.4 \text{ m s}^{-1}$ ; Garcez Faria et al. 2000) were generated by storm waves and winds with a predominant direction from the northeast. During these 3 days, waves measured at the 8-m depth array slowly increased in significant wave height from 1.7 to 2.3 m, in peak wave period from 6 to 7 s, and decreased in incident wave angle from  $38^\circ$  to  $10^\circ$ , relative to shore normal. Wind and wave conditions during daylight hours on each of these days were approximately steady state, and the depth contours near the measurement location were approximately straight and parallel.

The vertical structure of the flow field was measured with a vertical array of eight Marsh–McBirney, two-axis electromagnetic current meters (EMs) mounted on a vertical mast attached to a mobile sled. The EMs were distributed over the vertical starting at 0.23 m and extending upward to a maximum of 2.57 m above the bed. The EMs were horizontally displaced about 1 m from the sled in the alongshore direction. The sled was oriented so that the EMs were on the upcurrent side of the mean alongshore current to avoid flow contamination by the sled structure. The EMs were pre- and post-calibrated with 1.9% agreement in gain. The offset was determined in the field by reversing the orientation of the EMs at a time when alongshore currents were small and were found to agree within about  $0.01 \text{ m s}^{-1}$ . The sled orientation was measured with an onboard digital compass with an accuracy of about  $1^\circ$ ; however, the EMs themselves have about a  $5^\circ$  angle of uncertainty. Wave pressures and mean water levels were measured by an array of five pressure sensors configured in a 3-m square array with sensors at each corner of the sled and one in the middle. One pressure sensor was located at the base of the EM mast and is utilized in this study. Data from the EMs and pressure sensors were digitized onboard the sled at 36 samples per second and transmitted to shore via a fiber optic cable. The data are later low-pass filtered and resampled to 8 Hz for processing.

For the first run on each day, the sled was towed by the Coastal Research Amphibious Buggy (CRAB; Birkemeier and Mason 1984) to a location seaward of the bar (approximately 160 m from the shoreline) and detached. The beach profile along this line was obtained by measuring the CRAB location and elevation during the tow using an autotracking laser ranging survey system operated by the FRF staff. The instrumentation on the sled was recorded for a chosen sample time, after which a large forklift on the beach pulled the sled by an attached chain shoreward at 10–30-m increments for

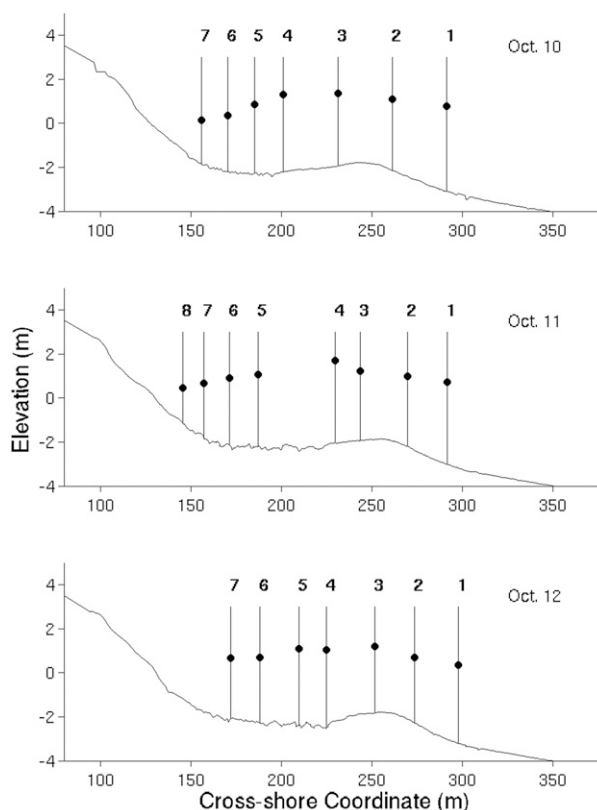


FIG. 1. Sled cross-shore locations along the measured beach profile for 10–12 Oct. The sequential station numbers are also indicated for each position on each day. The dots indicate the mean water level observed during each data run at each location.

subsequent runs. Each data run was nominally 1 h, allowing approximately 7–8 stations (i.e., positions across shore) spanning the surfzone to be occupied in an 8–10-h period. Each data run is referred to in the text by sequential numbers beginning with the most seaward run on that particular day. The measured beach profiles along the sled lines, and the positions with identification numbers of the sled locations during data runs, are shown in Fig. 1. The mean water level during the run is indicated, and because the sled locations were occupied sequentially, the tidal levels changed as the data runs progress throughout the day.

Wave breaking is important to the mixing of momentum over the vertical and thus the shape of the current boundary layer. During these 3 days, waves initially broke on the seaward flank and crest of the bar, reformed within the trough, and broke again on the shore. Wave breaking was monitored with video cameras and show, for example, that on the third run of 12 October approximately 80% of the waves broke on the bar while wave breaking reduced to less than 20% within the trough (Garcez Faria et al. 1998). The wave

TABLE 1. Statistics from the observations on a given date in October (day), station number (Sta.), and water depth  $h$  (m) with run length  $T$  (min). Velocity variables are in  $\text{m s}^{-1}$ . Phase and orientation variables are in degrees. Incident wave velocities,  $u_{\text{inc}}$  and  $v_{\text{inc}}$ , are taken from the top sensor in the most energetic frequency band (around  $f = 0.14$  Hz). Low-frequency velocities at the top and bottom,  $u_t$ ,  $u_b$ ,  $v_t$ , and  $v_b$ , correspond to  $f = 0.005$  Hz. Missing values for  $R_t$ ,  $R_b$ , and  $\theta_{E_b} - \theta_{E_t}$  are shown only when the stability is above the 95% significance level. Station 7 on day 10 and station 8 on day 11 were not used because too many sensors were coming in and out of the water at these very shallow locations.

Day	Sta.	$h$	$T$	DOF	$u_{\text{inc}}$	$u_t$	$u_b$	$\gamma_{u_b}^2$	$\phi_{u_b}$	$v_{\text{inc}}$	$v_t$	$v_b$	$\gamma_{v_b}^2$	$\phi_{v_b}$	$R_t$	$R_b$	$\theta_{E_b} - \theta_{E_t}$
10	1	3.86	74	44	0.392	0.142	0.085	0.62	-33.47	0.158	0.095	0.112	0.56	-4.66	0.09		
10	2	3.25	70	44	0.444	0.151	0.116	0.71	-9.43	0.264	0.092	0.127	0.37	-24.01	-0.20	0.12	-6.24
10	3	3.29	109	64	0.366	0.167	0.153	0.15	-33.66	0.179	0.131	0.163	0.59	3.46	-0.06	0.20	9.57
10	4	3.51	88	52	0.313	0.202	0.100	0.37	-30.93	0.182	0.119	0.116	0.39	-1.35	-0.10	0.02	28.05
10	5	3.14	79	48	0.285	0.207	0.120	0.74	-25.27	0.114	0.092	0.083	0.21	-43.39	0.37	0.03	23.24
10	6	2.57	71	44	0.273	0.127	0.082	0.50	3.86	0.089	0.097	0.088	0.67	13.43		0.49	
11	1	3.73	77	48	0.623	0.223	0.183	0.60	-25.80	0.216	0.142	0.152	0.55	-16.93	-0.10	0.06	-18.52
11	2	3.18	61	36	0.576	0.325	0.267	0.68	-28.71	0.188	0.120	0.190	0.43	-11.91	-0.20	0.22	11.07
11	3	3.14	31	20	0.485	0.269	0.186	0.36	-25.38	0.141	0.126	0.103	0.40	24.29	0.02	-0.03	4.43
11	4	3.74	60	36	0.297	0.233	0.080	0.37	-66.55	0.131	0.105	0.046	0.49	-2.36	-0.21	0.31	1.32
11	5	3.26	63	36	0.340	0.187	0.123	0.56	-42.18	0.115	0.097	0.088	0.45	30.88	0.00	0.28	-11.54
11	6	3.06	61	36	0.326	0.102	0.062	0.48	-1.47	0.132	0.121	0.077	0.47	-23.68		0.32	
11	7	2.49	59	36	0.204	0.094	0.060	0.25	-11.84	0.143	0.086	0.083	0.59	-7.03		0.32	
12	1	3.57	83	48	0.480	0.243	0.186	0.77	-13.44	0.132	0.122	0.137	0.62	-1.49	-0.02	0.23	-17.79
12	2	2.98	71	44	0.505	0.322	0.272	0.58	-29.51	0.173	0.152	0.178	0.16	51.04	-0.51	0.33	16.93
12	3	3.02	71	44	0.421	0.315	0.348	0.15	-18.06	0.197	0.183	0.147	0.21	2.00	0.25	-0.02	-13.81
12	4	3.56	60	36	0.302	0.276	0.175	0.37	-34.27	0.140	0.125	0.116	0.24	-46.58	0.21	-0.19	7.07
12	5	3.48	86	52	0.280	0.255	0.183	0.34	-14.27	0.123	0.111	0.110	0.46	-12.05	-0.09	-0.16	15.44
12	6	3.00	57	36	0.301	0.267	0.110	0.58	4.80	0.117	0.115	0.099	0.34	37.22	0.10	0.50	-33.75
12	7	2.74	54	32	0.223	0.124	0.090	0.58	8.19	0.069	0.102	0.079	0.51	9.48			

breaking intensity (e.g., fraction of waves breaking) reduced over the bar and maximum intensities moved slightly seaward at lower tides, whereas at higher tides the breaking intensity increased over the bar and extended further into the trough.

Spectral analysis is performed on time series of observed velocities and pressures. Spectra are computed by dividing the time series records into two non-overlapping lengths, applying a Hanning window to the time series, computing spectra over each demeaned and detrended ensemble member, and then smoothing the ensemble-averaged spectrum over a selected number of adjacent frequency bins. To avoid leakage arising from very-long-period oscillations not of interest to the present work, the lowest few (2–8) fundamental frequencies (determined by the record length) are eliminated from the ensemble-averaged spectra before band averaging, which is equivalent to a high-pass Fourier filter with a cutoff frequency  $\cong 0.0025$  Hz. The number of adjacent frequency bands averaged is determined such that the resolution  $\Delta f \cong 0.005$  Hz and the lowest spectral estimate has a center frequency as close to 0.005 Hz as possible. The degrees of freedom (DOF) are determined from the number of ensembles and bands averaged. The number of DOF varied from 20 to 64 as a function of record length at each sled position, ranging 31 to 109 min (Table 1). The 95% confidence intervals are computed for spectral estimates as well as 95%

significance levels and confidence intervals for cross-spectral coherence and phase, respectively (Hannan 1970; Priestley 1981). A Hanning data window is applied to each ensemble before computing the FFT to minimize spectral leakage. Several types of data windows were compared with good (but not identical) leakage properties, including a Hamming window, Kaiser–Bessel cosine taper, and first differencing followed by postcoloring, and found very little difference in phase (about  $\pm 3^\circ$ ), coherence (about  $\pm 0.02$ ), rotary coherence (about  $\pm 0.04$ ), and ellipse orientation (about  $\pm 3^\circ$ ), indicating that the results were insensitive to the choice of data window. Aliasing is not an issue as the Nyquist frequency (4 Hz) is much greater than the frequencies of interest.

Sea surface elevation spectra are obtained from pressure measurements at the base of the current meter mast by using linear wave theory to correct for depth attenuation (Guza and Thornton 1980). An example spectrum from sled station 2 on 12 October is shown in Fig. 2. At this location, seaward of the sandbar, the incident waves with spectral peak frequency of 0.14 Hz, are an order of magnitude more energetic than surface gravity waves at infragravity frequencies. Note that vorticity motions (at  $f \sim 0.005$  Hz) have very small surface signature and therefore do not contribute to the infragravity pressure spectrum. Also shown in Fig. 2 are the spectra for each component of velocity observed by each of the eight EMs. As expected, the cross-shore

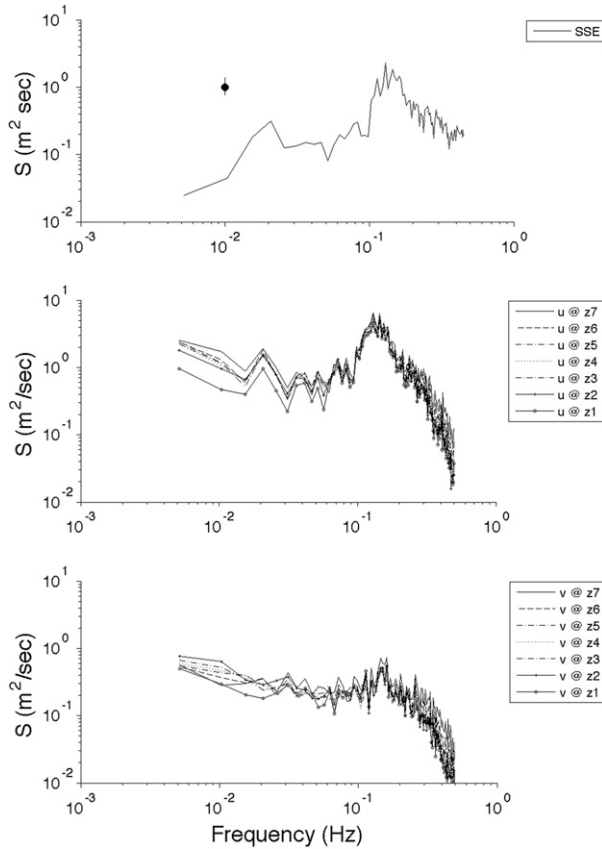


FIG. 2. Observed spectral densities from sled station 2 on 12 Oct of (top) sea surface elevation ( $\text{m}^2 \text{s}$ ) from a pressure sensor at the base of the current meter mast and of (middle) cross-shore and (bottom) alongshore velocities ( $\text{m}^2 \text{s}^{-1}$ ) from each current meter (with position in the vertical indicated in the legend). The spectra are plotted on log-log scale where the horizontal axis is frequency (Hz). Spectra are computed with 44 degrees of freedom with smoothed frequency bandwidth of 0.005 Hz. The 95% confidence interval is shown in the upper panel.

component of the incident sea and swell wave velocities is much more energetic than the alongshore component. The energy spectra at infragravity frequencies have shapes qualitatively consistent with the nodal structure of a standing (in the cross shore) gravity wave field (Guza and Thornton 1985). Unlike the infragravity pressure spectrum, the infragravity velocity spectra increase as frequency decreases for both components of the flow, consistent with a relative increase in energy of vortical motions relative to surface gravity waves as the periods get longer (Oltman-Shay et al. 1989).

The relative fraction of shear instability energy (or equivalently applied to a generic class of vorticity motions) to surface gravity wave energy can be estimated by integrating the velocity and pressure spectra over a given frequency range  $f_1 < f < f_2$  to compute the velocity to pressure variance ratio  $Q$ :

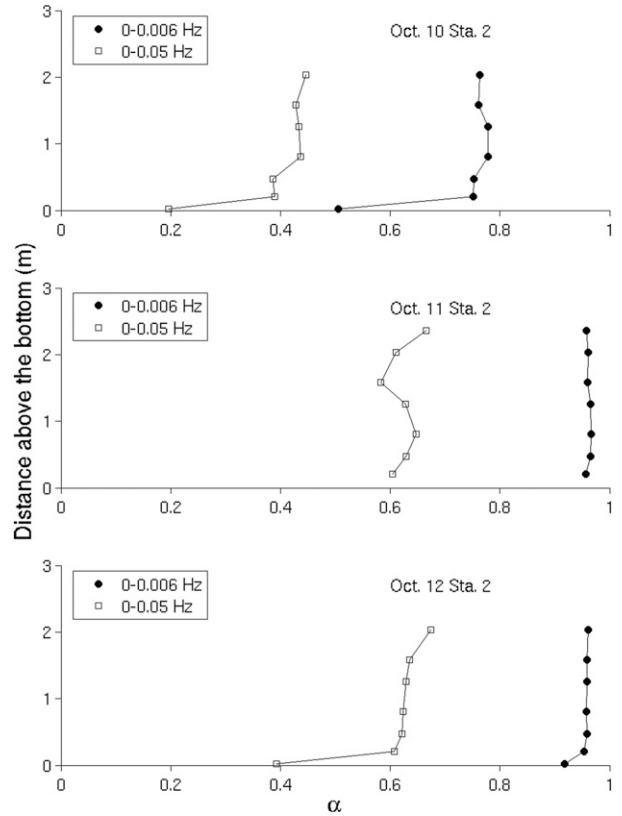


FIG. 3. Fraction of vorticity wave energy  $\alpha$  as a function of distance above the bottom (m) for the total infragravity frequency band ( $0.0025 < f < 0.05$  Hz; open squares) and for the very low frequencies ( $0.0025 < f < 0.0075$  Hz; filled circles) at sled station 2 from (top) 10 Oct, (middle) 11 Oct, and (bottom) 12 Oct.

$$Q = \frac{\langle u^2 \rangle + \langle v^2 \rangle}{\langle p^2 \rangle} \frac{g}{h}, \quad (1)$$

where  $g$  is gravity,  $h$  is the water depth, and  $\langle p^2 \rangle$ ,  $\langle u^2 \rangle$ , and  $\langle v^2 \rangle$  denote the pressure head (sea surface elevation), cross-shore velocity, and alongshore velocity spectra integrated over the frequency band defined by  $f_1$  and  $f_2$  (Lippmann et al. 1999). For an infragravity wave field consisting only of a broad distribution of edge and leaky surface gravity waves,  $Q = 1$ . When vorticity motions are present,  $Q > 1$  because they do not contribute to the pressure spectrum. The fraction of the energy spectrum consisting of vorticity motions  $\alpha$  is estimated by

$$\alpha = 1 - \frac{1}{Q}. \quad (2)$$

When vorticity motions are absent,  $\alpha = 0$ , and in the limit for an energy spectrum consisting entirely of vorticity motions,  $\alpha = 1$ .

Observed  $\alpha$  from sled station 2 are shown in Fig. 3 for each of the 3 days analyzed using each EM



independently with the pressure sensor at the base of the EM stack. Two frequency ranges are examined. The first spans the low and infragravity frequency bands ( $0.0025 < f < 0.05$  Hz), and the second only includes the lowest-frequency bin in the spectra ( $0.0025 < f < 0.0075$  Hz). At sled station 2 for each of the 3 days, the sled was located on the seaward flank of the bar within the surfzone where there is generally strong positive shear in the alongshore current profile, and thus vorticity motions are expected in the presence of the observed energetic alongshore currents. The data (Fig. 3) indicate that about 40%, 60%, and 60% of the total low and infragravity wave energies on the seaward flank of the sandbar are contributed by vorticity motions on 10, 11, and 12 October, respectively. The data also show that vorticity motions contribute about 75%, 95%, and 95% of the energy in the very lowest frequencies ( $f < 0.006$  Hz).

The unknown edge wave mode/leaky wave mix and the complex cross-shore nodal structure in standing infragravity waves complicates the interpretation of the data when looking at specific frequency bands that include a significant fraction of surface gravity waves. Thus, our analysis will be restricted to the frequency band centered at 0.005 Hz and in doing so will consider only the vertical structure of vorticity motions.

At times, the uppermost EM was coming into and out of the water as waves passed the sled location. These data are eliminated from the analysis. While conditions are nearly stationary over the approximately 1-h data runs, the data acquired at different locations on the same day are not synchronous and the surfzone width, local water depths, and mean alongshore current profile evolve throughout the day. A summary of data runs is given in Table 1, including date, sled station number, water depth  $h$  (m), run duration  $T$  (minutes), and DOF used in the spectral calculations. Also included in Table 1 are incident wave root-mean-square (rms) velocities at the peak incident frequency (nominally at 0.14 Hz)  $u_{\text{inc}}$  and  $v_{\text{inc}}$ ; rms velocities of vorticity motions ( $f = 0.005$  Hz) at the top,  $u_t$  and  $v_t$ , and bottom,  $u_b$  and  $v_b$ ; squared coherence,  $\gamma_{u_b}^2$  and  $\gamma_{v_b}^2$ , and phase,  $\phi_{u_b}$  and  $\phi_{v_b}$ , between the top and bottom sensors; rotary coefficients at the top and bottom  $R_t$  and  $R_b$ ; and the change in ellipse orientation from top to bottom  $\theta_{E_b} - \theta_{E_t}$ .

Observations at the sled locations were obtained sequentially through each tidal cycle and so do not define the mean current profile across the surfzone. However, mean currents were also measured during Duck94 with a fixed cross-shore array of near-bottom current meters that spanned the surfzone. Feddersen et al. (1996) show the cross-shore profile of the observed mean alongshore current  $V(x)$  from 10 to 11 October at high and low tides

and also indicate the location of the maximum longshore current  $V_{\text{max}}$  relative to the bar crest location for 10–12 October. Our observations occur over about 8–10 h with high tide occurring at about the middle of the runs. Feddersen et al. show that  $V_{\text{max}}$  occurs between about  $x = 210$  m and  $x = 250$  m in the FRF coordinate system. Thus, sled positions 4–7 on 10 October, 5–8 on 11 October, and 5–7 on 12 October are shoreward of  $V_{\text{max}}$ , and sled positions 1–2 on all 3 days are seaward of  $V_{\text{max}}$ . Observations of the mean current profile for midday on 12 October are also shown in Newberger and Allen (2007) and are consistent with the values of  $V_{\text{max}}$  for that day given by Feddersen et al. (1996). These observations allow us to qualitatively place our observations in the context of the gross behavior of the mean alongshore current profile.

The discussion is focused on two representative locations on each of the 3 days: one location seaward and one shoreward of the bar crest and  $V_{\text{max}}$  location. For each day, the vertical structure is examined at sled location 2 on the seaward flank of the sandbar and sled location 5 in about the middle of the bar–trough profile. The depth of water at these locations insures that the uppermost sensor is always in the water. These data are representative of the changes that occur across the barred surfzone.

### 3. Results

To place the observations in context of other motions, the well-known behavior in shallow water of the vertical structure of the incident sea-swell wave field is examined first. In particular, significant vertical structure is not expected above the thin near-bed oscillatory boundary layer at incident wave frequencies in the shallow-water depths of the surfzone where the sled was positioned. Thus, our methodology can be verified with the incident wave observations, and any low-frequency vertical structure not previously observed can be compared qualitatively in magnitude to the observed higher-frequency structure with well-known theoretical behavior.

The analysis follows two lines: First, the spectral energy levels and cross-spectral squared coherences (henceforth, simply coherence) and phases over the vertical are compared for each horizontal velocity component separately. Second, the vertical variation in rotary components is examined that describes the rotational nature of the motions, including rotary coherence, ellipse orientation, and rotary coefficient (following Gonella 1972). These parameters are discussed in more detail later.

The cross-spectra obtained at sled station 2 on 11 October between EMs at position 4 (1.01 m above the

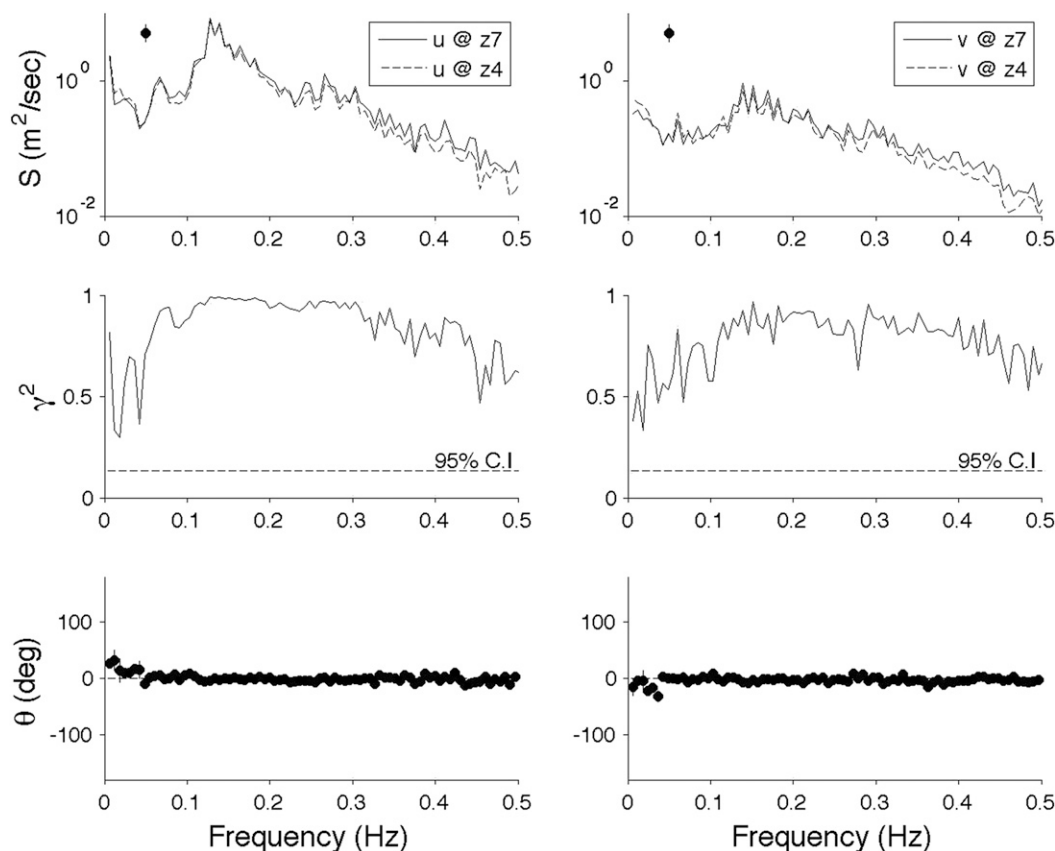


FIG. 4. Observed cross spectra between sensors separated 1.2 m in the vertical located at sled station 2 on 11 Oct for the (left) cross-shore and (right) alongshore flow components. (top) Spectral densities from two current meters (4 = dashed lines; 7 = solid lines). The (middle) coherence and (bottom) phase spectra. The spectra are computed over a 1-h period with 44 degrees of freedom. The smoothed spectral bandwidth is 0.006 Hz. The 95% confidence intervals are shown in the upper panels. The 95% significance level for zero coherence is shown with the dashed line in the middle panel. The corresponding 95% confidence intervals for the phase estimates are shown with the vertical line through each phase data point (the sizes of phase symbols are often larger than confidence intervals).

bed) and 7 (2.24 m above the bed), separated by 1.2 m vertically, are shown for each component of the velocity in Fig. 4. The shape of the spectra is nearly identical over most of the incident sea swell and higher frequencies, with coherences nearly equal to unity over a majority of the incident wave band. Phase shifts at incident and higher frequencies are generally equivalent to time lags less than the sampling interval (0.125 s) and thus are not distinguishable from zero-phase shift. At frequencies below the incident wave peak, the coherence shows a marked drop. At given nodes in the standing gravity wave field, a reduction in coherence at horizontally collocated sensors is expected (Guza and Thornton 1985); however, this reduction is expected only at specific frequencies, not the general decay in coherence with decreasing frequency as seen clearly in the alongshore velocity cross spectrum. Furthermore, there is a distinctly nonzero-phase shift at the lowest frequencies

for both components of the velocity. Although the coherence drop at surface gravity wave nodes is expected (Guza and Thornton 1985), the phase shift is not, particularly for sensors located within a meter vertically of one another.

In tidal flows on the continental shelf, the bottom boundary layer modifies the flow profile in such a way that a rotational change is imparted on the flow over the vertical (Prandle 1982; Soulsby 1990). In the companion paper (Lippmann and Bowen 2016, hereinafter Part II), the theoretical development follows that by Prandle for tidal flows where the vorticity effect of Coriolis is replaced by a horizontally sheared alongshore current, and it is expected that a rotational change will occur in the flow field influenced strongly by a bottom boundary layer. Thus, rotary spectra are computed following Gonella (1972) using both components of the flow observed with each EM over the vertical.

There are three basic rotary parameters (Gonella 1972): The first is the rotary coherence  $\gamma_R^2$  that describes how coherently the cross-shore and alongshore components of the velocity are oscillating. Analogous to the cross-spectral coherence, the rotary coherence is bounded by 0 and 1 and has well understood significance levels for zero coherence. The second parameter describes the orientation of the ellipse major axis  $\theta_E$  inscribed by the flow in phase space. For incoherent rotary motion (i.e., rotary coherence below the defined significance level), the ellipse orientation has no meaning and the flow does not have a stable rotary motion (the rotary coherence is sometimes referred to as the rotary stability parameter; Gonella 1972). The third parameter is the rotary coefficient  $R_c$  that describes the rotational nature of the flow at that particular frequency and is bounded by  $-1$  and  $1$ . When the rotary coherence is significant, then the rotary coefficient describes the sense of rotational motion. When the coefficient is zero, there is no rotational motion and the flow oscillates along a trajectory aligned with the direction indicated by the ellipse orientation. When the coefficient is nonzero, there is a sense of elliptical rotation in the anticlockwise (negative coefficient) or clockwise (positive coefficient) directions with the orientation parameter describing the direction of the semimajor axis of the ellipse. When the coefficient approaches  $\pm 1$ , the rotation becomes circular.

The rotary spectral parameters for EM number 7 obtained at sled station 2 on 12 October are shown in Fig. 5. At the spectral peak of incident wave frequency (about  $f = 0.14$  Hz), the rotary coherence is high (about 80%), the ellipse orientation is at some angle near zero (indicating nearly shore-normal wave approach), and the rotary coefficients are nearly zero (indicating motion predominantly back and forth along the trajectory described by the ellipse orientation). The incident waves are generally not rotary, and if there is some nonzero wave direction relative to the shore normal, the cross- and alongshore velocities will describe a coherent oscillating motion along the direction of predominant wave approach. At the lower, infragravity frequencies, the rotary coherence drops off rapidly with frequency and then increases toward the lowest-frequency end of the spectrum. At these lower frequencies with coherent rotary motion, the ellipse orientation is at some angle, and the rotary coefficient is distinctly nonzero. In the example shown in Fig. 5, the rotary coefficient is about  $-0.5$  at the lowest frequency at  $f = 0.005$  Hz, indicating an elliptical rotary motion progressing in the anticlockwise direction with the semimajor axis oriented at some small angle to the cross-shore direction.

In the following, the variation of cross-spectral and rotary parameters with depth are examined at the

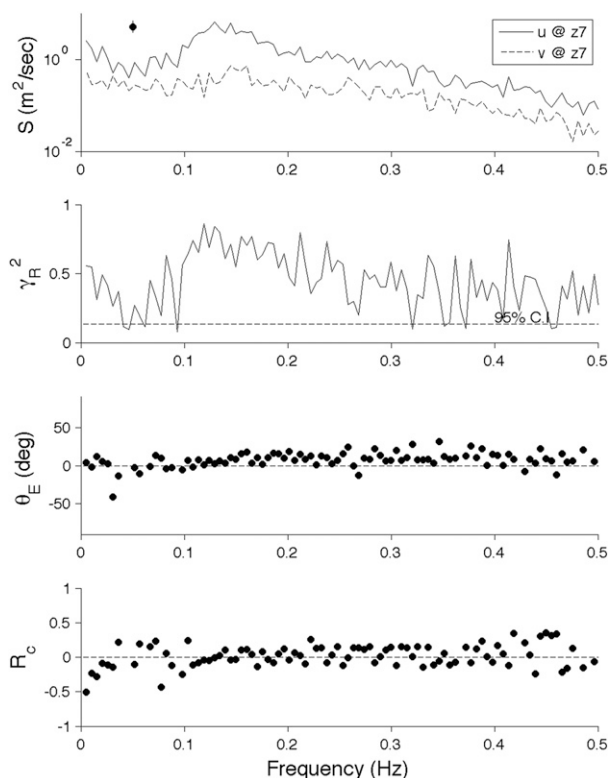


FIG. 5. Observed rotary spectra at current meter 7 at sled station 2 on 12 Oct. (top) Spectral densities from the cross-shore (solid lines) and alongshore (dashed lines) components of the flow. The (second from the top) rotary coherence, (second from the bottom) ellipse orientation, and (bottom) rotary coefficient spectra are also shown. The spectra were computed from a 71-min record with 44 degrees of freedom. The 95% confidence interval for the spectra is shown in the upper panel. The smoothed frequency bandwidth is 0.005 Hz. The 95% significance level for zero rotary coherence is shown with the dashed line.

incident wave peak frequency band and the low-frequency band centered at  $f = 0.005$  Hz. Specifically, the coherence and phase shift relative to the uppermost sensor for each component of the velocity are compared separately and then examined for how the rotary coherence, ellipse orientation, and rotary coefficient vary with depth.

First, the vertical structure of the spectral incident wave peak ( $f = 0.14$  Hz) observed at sled station 2 on 11 October is examined. The vertical structure in rms amplitudes  $u_{\text{rms}}$  and  $v_{\text{rms}}$ , coherence  $\gamma_u^2$  and  $\gamma_v^2$ , and phase  $\theta_u$  and  $\theta_v$  (relative to the uppermost sensor), and rotary parameters are shown in Fig. 6 as a function of distance above the bottom. The rms amplitudes decay slightly with depth (except right at the bottom) in accord with linear wave theory (dashed-dotted line). For both components of the flow, the coherence is uniform and near unity throughout the water column except at the



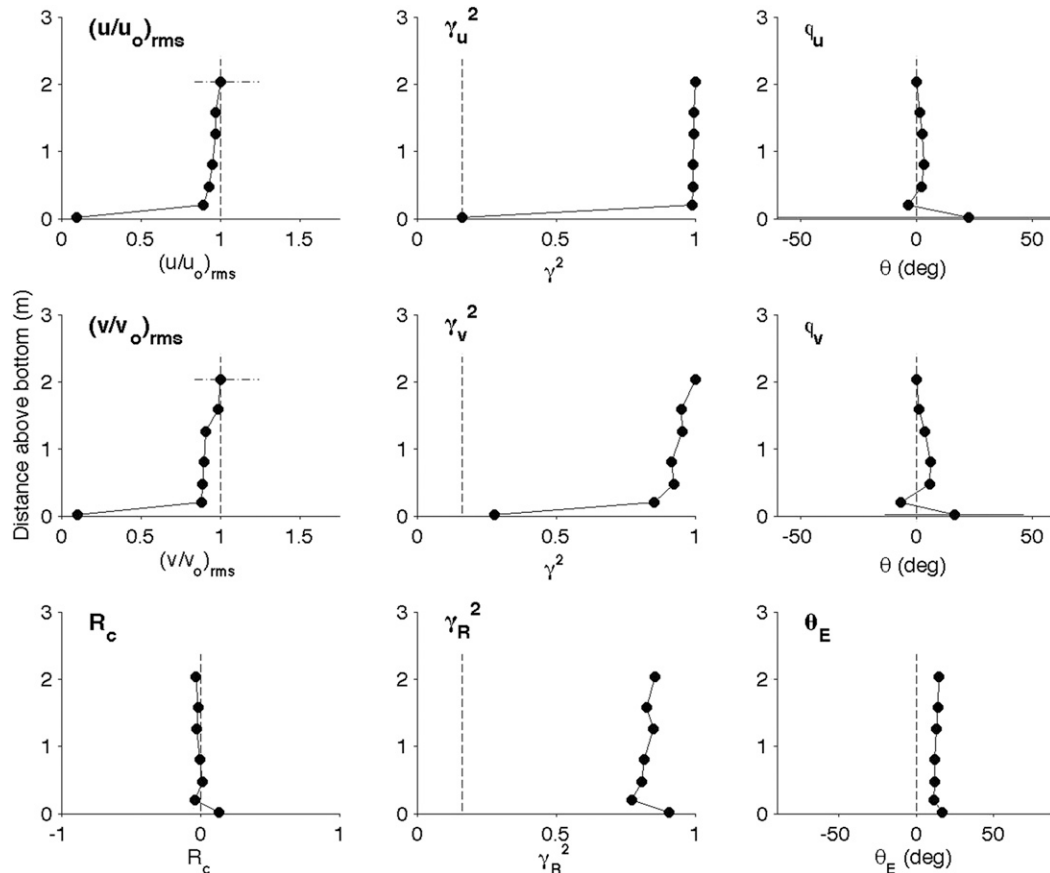


FIG. 6. Vertical structure of (top) cross-shore velocity, (middle) alongshore velocity, and (bottom) rotary parameters at the peak incident wave frequency ( $f = 0.14$  Hz) from sled station 2 on 11 Oct. (left top and middle) RMS velocities relative to the uppermost sensor as a function of distance above the bottom (m). (center top and middle) Coherence relative to the uppermost sensor. (right top and middle) Phase ( $^{\circ}$ ) relative to the uppermost sensor. Negative phases indicate the bottom is leading the surface. (left bottom) Rotary coefficient, (middle bottom) rotary coherence, and (right bottom) rotary ellipse orientation ( $^{\circ}$ ) as a function of distance above the bottom. The spectra were computed over 61 min record with 36 degrees of freedom. The 95% confidence interval for the velocities is shown as the horizontal dashed–dotted lines. The 95% significance level for zero coherence is shown with the dashed line in the three center panels. The corresponding 95% confidence intervals for the phase estimates are shown as the horizontal lines through the data points (for the data here the confidence intervals are within the circle).

bottom, and there is no phase shift larger than that resolved by the sampling frequency ( $\leq 6^{\circ}$ ), except near the bottom where coherence is low. The rotary coherence is significant (about 80%), and the ellipse orientation is nonzero and uniform with depth (indicating a predominant wave angle of about  $10^{\circ}$  to the north of shore normal at the FRF field site). The rotary coefficient is about zero throughout the water column, indicating a nonrotary oscillating motion along the trajectory described by the ellipse orientation (i.e., along the direction of wave approach).

Aside from energy and wave angle variations associated with wave transformation across the barred surf-zone, there are no real differences between the

observation shown in Fig. 6 and the other sled stations on any of the 3 days examined. Thus, the remainder of the analysis is concentrated on the low-frequency motions centered at  $f = 0.005$  Hz (Figs. 7–12) shown in the same layout as for the incident wave example (Fig. 6). Results are shown from sled station 2 (on the seaward flank of the sandbar seaward of  $V_{\max}$ ) for 10–12 October (Figs. 7–9) and from sled station 5 (in the trough of the sandbar shoreward of  $V_{\max}$ ) for 10–12 October (Figs. 10–12).

For the data on the seaward flank of the sandbar (sled station 2; Figs. 7–9), the rms cross-shore flow shows a nearly uniform distribution in the upper part of the water column and attenuation toward the bottom,

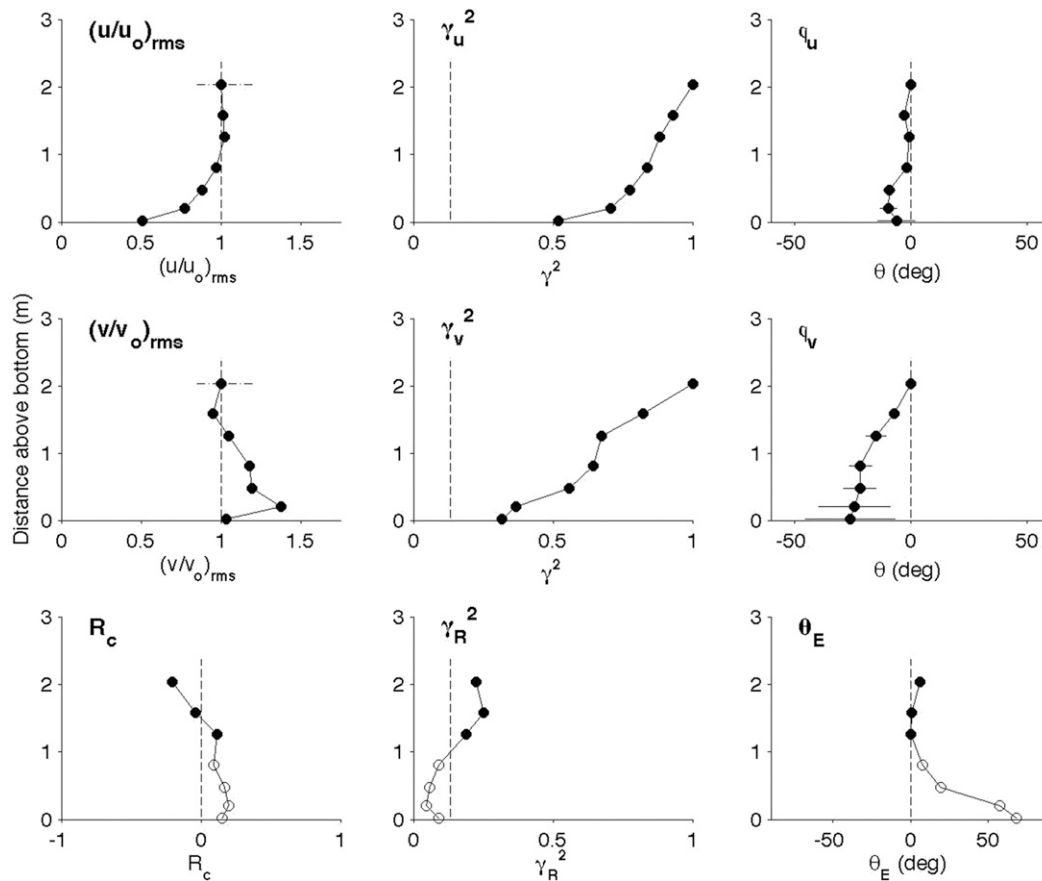


FIG. 7. As in Fig. 6, but for low-frequency motions ( $f = 0.005$  Hz) from sled station 2 on 10 Oct (44 degrees of freedom). Estimates of parameters with coherences below the 95% significance level are shown with open circles.

qualitatively consistent with the presence of a bottom boundary layer and (possibly) mixing by breaking waves in the upper part of the water column. Interestingly, the rms alongshore flow increases toward the seabed. More striking is the sharp drop off in coherence with depth for both components of the flow, decaying in an approximately linear manner up to 50%–80% over the water column. The phase relative to the surface shifts approximately linearly with depth by as much as  $10^\circ$  to  $50^\circ$  over the water column. In general, the phase shifts are negative (indicating a phase lead at the bottom); however, there is also evidence that the phase can change sign, as indicated in Fig. 9 for the alongshore component of the flow observed on 12 October. At this location, the flow in the lower half of the water column is nearly incoherent from the surface, with poorly constrained phase (indicated by the weak coherence and large confidence intervals on the phase).

The rotary coherence is in general significantly nonzero. The ellipse orientation is also nonzero and appears to shift (rotate) with depth to more positive angles toward the bottom, suggesting a turning of the flow field

increasing toward the seabed. The rotary coefficients are generally nonzero and vary vertically with a sign change observed at this location on each of 3 days examined. This sign change indicates that the rotational direction changes in the vertical, and coupled with the vertically varying ellipse parameter, suggests a complex flow behavior, whereby the flow field is turning and changing rotational nature over just 2 m in the vertical. This rotational change between the near surface and the near bed flow is consistent with the rapid drop off in coherence, particularly in the alongshore component of velocity.

Similar behavior is observed in velocity data obtained in the trough of the sandbar (Figs. 10–12). In this region, the amplitude decay in the cross-shore component of the flow occurs throughout the water column, indicating a well-developed boundary layer extending over the entire water column. The reduction in wave breaking in this region limits the vertical mixing near the surface. Interestingly, the alongshore component of the flow in this region does not vary much with depth. The coherence again drops off sharply with depth, and the

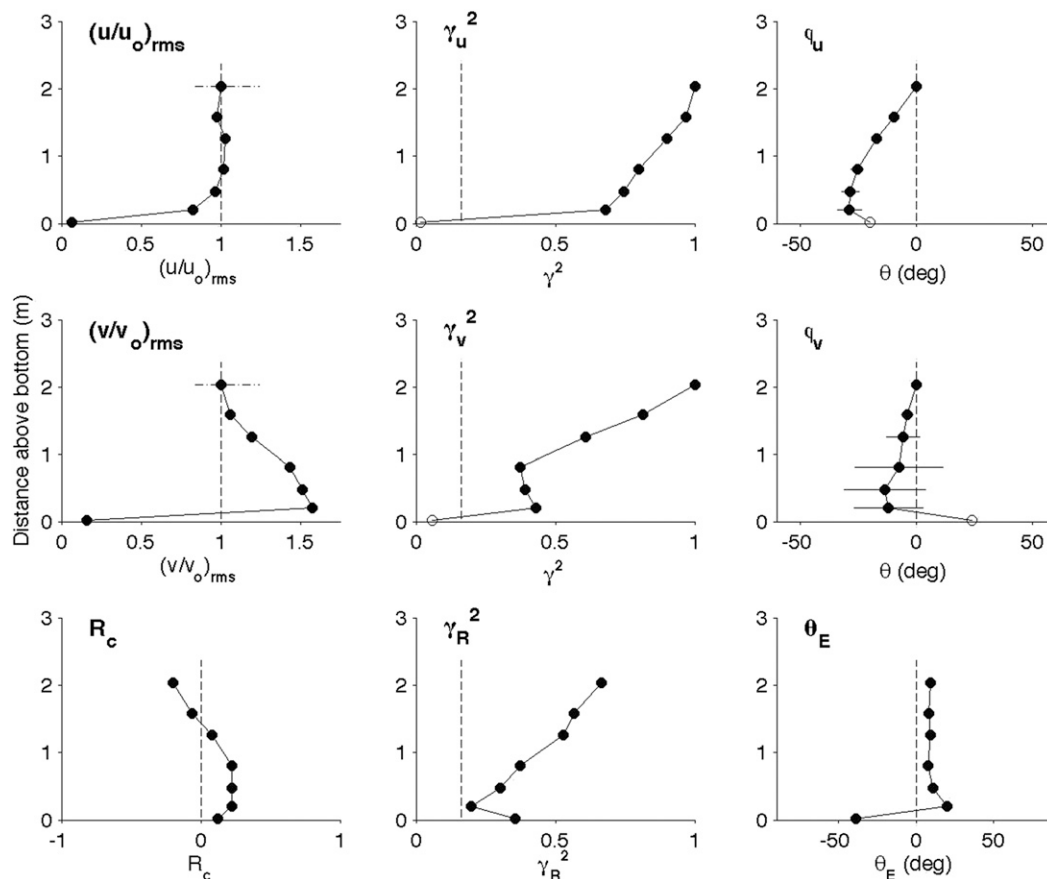


FIG. 8. As in Fig. 7, but on 11 Oct (36 degrees of freedom). Phase confidence intervals are not computed for incoherent values.

phase shift can be positive or negative. The cross-shore component of the flow at the bottom tends to lead the surface in all observed cases, but the alongshore component of the flow can either lead or lag depending on the location in the surfzone relative to the mean alongshore current profile. The rotary coherences are again significantly nonzero, and the ellipse orientations indicate a turning of the flow with depth. The rotary coefficient is nonzero and varies vertically with depth but is not observed to change sign as it did in the observations on the seaward flank of the sandbar.

A summary of relevant parameters for all data runs is given in Table 1. The data show that the low-frequency ( $f = 0.005$  Hz) oscillations are about 25%–100% that of the peak incident wave rms velocities, tending to relatively increase toward shore as incident waves are attenuated by breaking but dependent on the location relative to maximum mean alongshore current. Phase shifts over the vertical are large for both cross-shore and alongshore components of velocity and change sign in a manner that is not entirely clear from the data. The

motions are rotary with a sense that changes in the vertical and in space, with major axis ellipse orientation rotating down in the water column in both clockwise and anticlockwise directions. The coherence drops off significantly over the shallow depths, likely due to the complex phase structure and rotational nature of the flow.

#### 4. Discussion

The observations show a large drop in coherence over the water column for vorticity motions with 200-s oscillations as well as significant phase shifting up to  $50^\circ$  over the vertical (amounting to about a 30-s lag time between the current reversals at the surface relative to the bottom). Observations of the flows separated by about 1 m in the vertical can be nearly incoherent. This is likely a result of the complex rotational behavior observed, with the sense of rotation (clockwise or anticlockwise) varying vertically and at times changing sign at the same horizontal location. This complex behavior

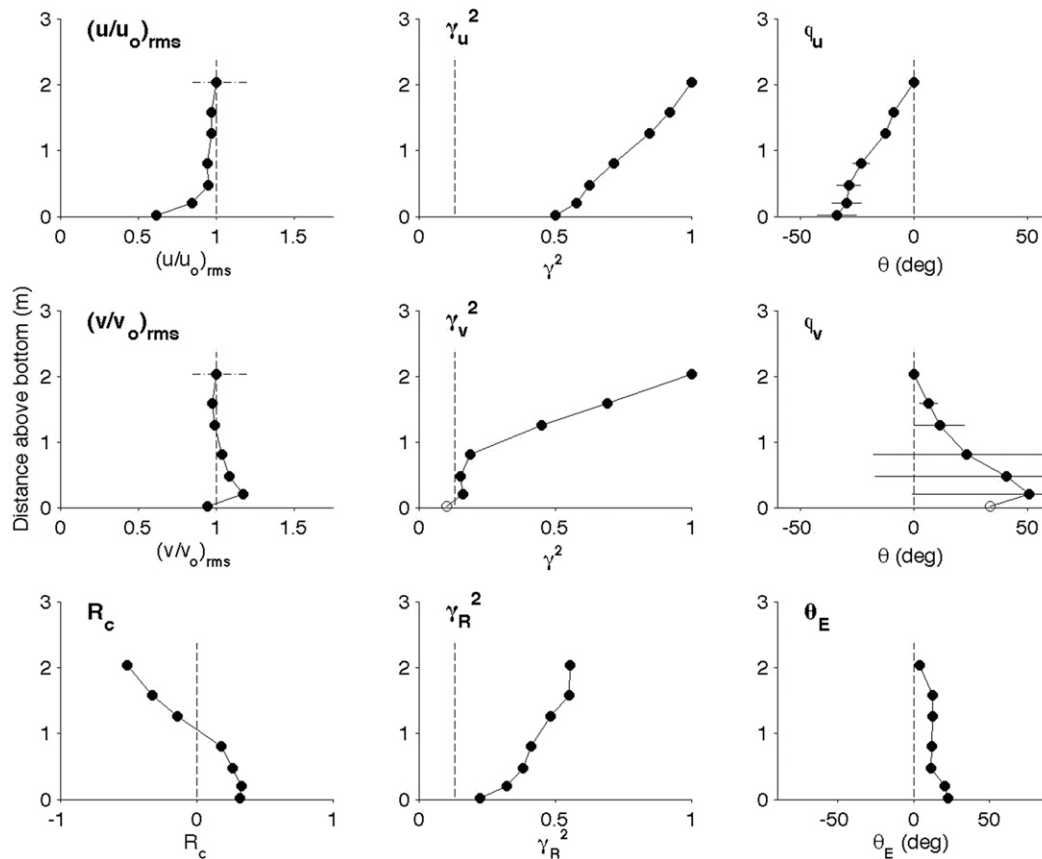


FIG. 9. As in Fig. 7, but on 12 Oct (44 degrees of freedom).

has not been previously observed in low-frequency motions in the surfzone.

Observations of vorticity motions have been made on natural beaches since the late 1980s (Oltman-Shay et al. 1989) and are usually quantified with frequency–wavenumber spectra estimated from alongshore arrays of EM current sensors spanning a couple hundred meters or so. The nature of the observing arrays relies on the energy, coherence, and phase relationships of the lagged EMs in the array. The observed decay in energy, rapid drop in coherence, and linear phase shift over the vertical suggest that the distance the sensor is located above the bottom is as important a consideration as the distance separating the sensors and that in order to examine the spatial variation of vorticity motions, sensors separated horizontally should optimally be at the same depth. In general, this has not been the case for typical observing arrays deployed in field experiments. However, because vorticity motions are generally well resolved with extensive spatial arrays of current meters mounted near the bottom (e.g., Oltman-Shay et al. 1989; Noyes et al. 2004; and others), it suggests that having the sensors in the array deployed at nearly the same depth is

sufficient to resolve the spatial character of the wave field. The vertical coherence decay and phase shifts may influence the energy levels computed at these low, energetic frequencies dominated by vorticity motions, but the frequency–wavenumber signature appears to be retained.

Of particular (and considerable) interest is the effect of vorticity motions on mixing momentum across the surfzone and its impact on the cross-shore distribution of the turbulence and other flow properties. Dodd and Thornton (1990) showed that if shear instabilities are to exist, then horizontal momentum mixing must take place. This mixing can be very complex as shown by nonlinear model simulations of the vorticity fields associated with shear instabilities (Allen et al. 1996; Slinn et al. 1998; Ozkan-Haller and Kirby 1999) or other vorticity motions (Long and Özkan-Haller 2009; MacMahan et al. 2010; Clark et al. 2012; Geiman and Kirby 2013; Feddersen 2014). All of these studies assume a two-dimensional horizontal flow uniform with depth. The impact of vertical variation in the vorticity motions, as observed in this work, was not considered.

Svendsen and Putrevu (1994) showed that nearshore mean currents with vertical shear could mix momentum

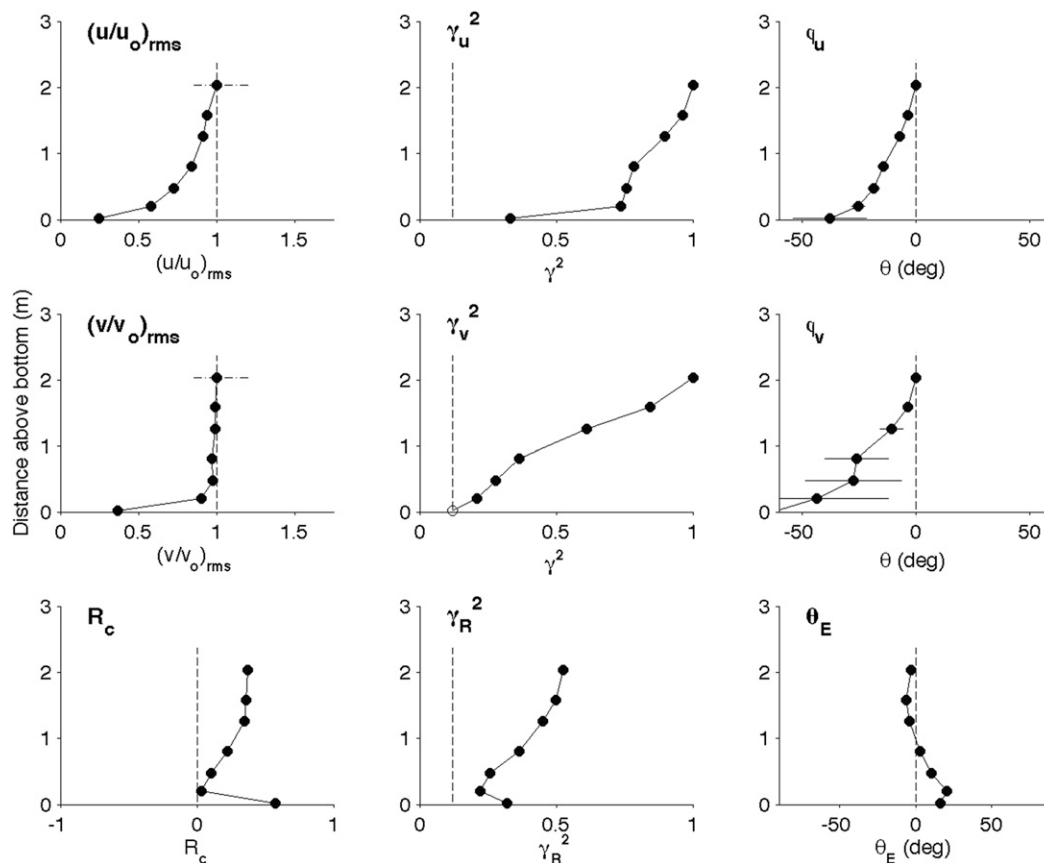


FIG. 10. As in Fig. 6, but for low-frequency motions ( $f = 0.005$  Hz) from sled station 5 on 10 Oct (48 degrees of freedom). Estimates of parameters with coherences below the 95% significance level are shown with open circles.

horizontally with enough strength to modify the along-shore current profile. In a similar manner, Zhao et al. (2003) examined the quasi-three-dimensional vertical structure of nearshore currents when simulating shear instabilities; that is, the averaging time for the mean currents was within the shear instability frequency band. This mean vertical structure is allowed to interact with the shear instabilities that in turn modify the current structure on the time scale of the instabilities. They found that the work done by the vertical momentum mixing on the instabilities extracts kinetic energy from the depth-averaged shear energies and transfers it to the depth-varying part of the currents. The amount of the mixing depends on the strength and vertical shear of the currents as well as the bandwidth under consideration.

Zhao et al. (2003) also examine modeled instantaneous velocity profiles and found that shear instabilities varied over the vertical with sometimes higher velocities at the bed and with flows at the surface  $180^\circ$  out of phase with flows near the bottom. The phase, coherence, or rotational vertical structure was not considered. Their modeled vertical structure was primarily

observed far seaward of the nearshore sandbar, whereas our observations are within the surfzone in the vicinity of the bar–trough region, complicating comparison with their results. In any case, Zhao et al. conclude that shear instabilities show a depth dependency that arises in the model due to the dispersive mixing defined by Putrevu and Svendsen (1995). Our observations of the vertical variation in energy, rotational motion, and turning of the flows suggest that mixing may be substantial. The strength of this mixing is the subject of ongoing research.

## 5. Conclusions

Field observations obtained at the 1994 Duck94 nearshore field experiment are used to examine the vertical structure in energy, phase, and rotation of low-frequency motions. Measurements of the flow field are made from a vertical array of two-axis electromagnetic current meters mounted on a mobile sled that is positioned at various locations across the surfzone through an 8–10-h period. Three previously well-studied days are examined from Duck94 (10–12 October; Garcez Faria



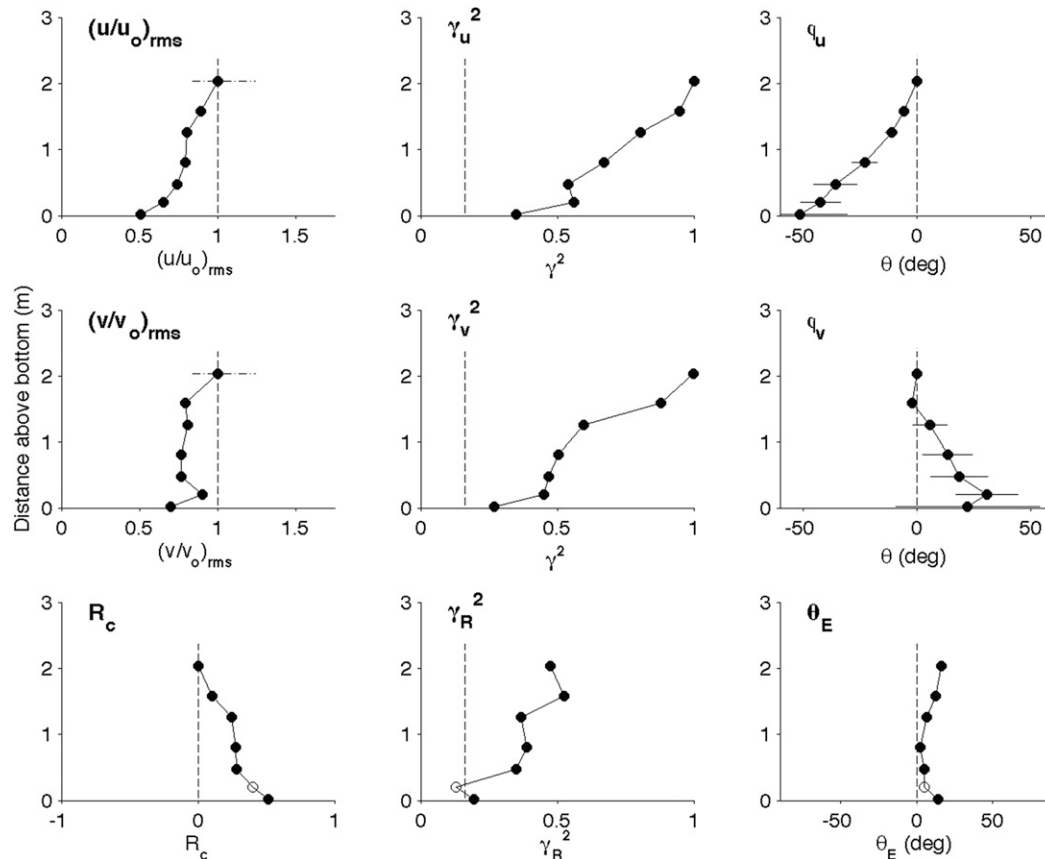


FIG. 11. As in Fig. 10, but on 11 Oct (36 degrees of freedom).

et al. 1998, 2000) during storm wave conditions when strong alongshore currents were present.

Low-frequency spectra consist of a mix of surface gravity waves and vorticity motions. Owing to the complex cross-shore nodal structure that depends on wave frequency associated with standing surface gravity waves, the discussion is limited to the lowest frequency centered at  $f = 0.005$  Hz. At this low frequency, most of the energy (75%–95%) is associated with vorticity motions [as determined by the integrated spectral approach of Lippmann et al. (1999)].

Observed rms amplitude variations in the cross-shore component of the flow ( $f = 0.005$  Hz) seaward of the sandbar suggests the presence of a bottom boundary layer. The alongshore component of the flow increases slightly near the bottom, seaward of the sandbar, and is nearly uniform over the water column inside the surf-zone. The coherence between each of the vertically separated sensors and the uppermost sensor drops off quickly for both components of the low-frequency flow, with as much as 70%–80% coherence drop across the water column. Sensors separated only by a meter or so

can show strong reduction in coherence even at these long-period motions. Additionally, the phase relative to the uppermost sensor shifts approximately linearly over the water column, with as much as  $50^\circ$  lags from top to bottom. The bottom sensors sometimes lead and sometimes lag the surface, depending on their position in the cross-shore relative to the sandbar and the mean alongshore current profile. In Part II, theoretical considerations suggest that the relative magnitudes (and direction) of the alongshore current, wavenumber, wave frequency, and cross-shore shear of the mean alongshore current determines the sign of the phase shift. The theory is complicated by the poorly determined eddy mixing and bottom drag coefficients and the nature of the phase-shifting behavior is not well constrained by observation.

Spatially and vertically varying phase structure describes rotary motions that vary across the surfzone. The rotary coefficients are generally nonzero, indicating that the low-frequency motions have rotational nature, with direction (cyclonic or anticyclonic) that depends on the position of the sensors relative to the sandbar and the

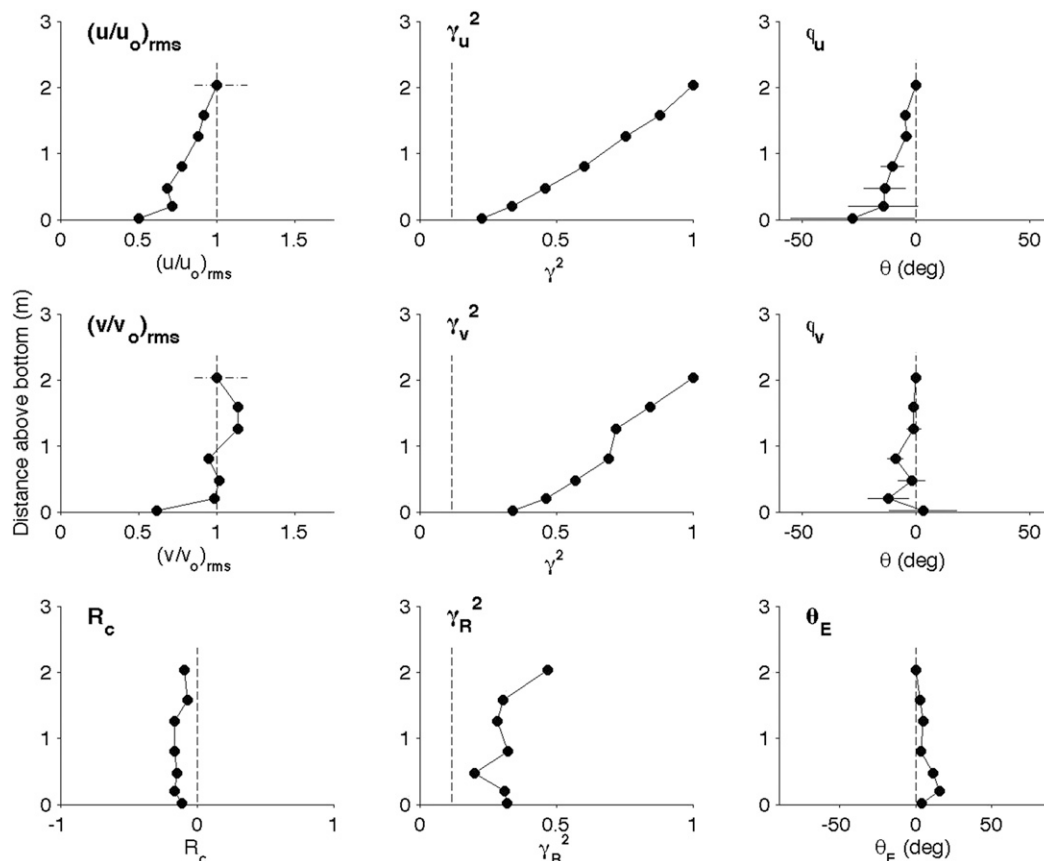


FIG. 12. As in Fig. 10, but on 12 Oct (52 degrees of freedom).

alongshore current profile. The rotary coefficients are generally not uniform with depth and can change sign in the vertical, indicating a strong rotational change in the motions over the shallow depths. The ellipse orientations also vary with depth, indicating a turning of the flows toward the bottom. The observed behavior is qualitatively predicted by simple boundary layer theory (discussed in Part II).

At incident wave frequencies, the vertical variation in phase and rotational motion is uniform with depth, as expected from the well-known behavior of shallow-water waves with thin bottom boundary layers. The relatively long-period oscillations examined (at 200 s) relative to the incident periods (about 7 s) allows for the development of a bottom boundary layer that extends over the entire water column. Although not examined in great detail in this work, the boundary layer development is expected to be more significant as the wave periods increase, irrespective of the nature of the motion (be it vorticity motions or surface gravity waves). Based on previous modeling considerations (Zhao et al. 2003), the impact of the vertical variation

within the low-frequency oscillating boundary layer on horizontal mixing within the surfzone is expected to be considerable.

**Acknowledgments.** We wish to thank the many folks who assisted in obtaining a valuable dataset, in particular the FRF staff led by Bill Birkemeier and Antonio Garcez Faria, Jim Stockel, and Rob Wyland of the Naval Postgraduate School. We thank the anonymous reviews for their thoughtful and insightful comments that greatly improved the paper. This work was funded by the Office of Naval Research (ONR) under Contracts N000140210238 and N000141410557 (TCL) and N0001405WR20150 and N0001405WR20385 (EBT and TPS).

## REFERENCES

- Allen, J. S., P. A. Newberger, and R. A. Holman, 1996: Nonlinear shear instabilities of alongshore currents on plane beaches. *J. Fluid Mech.*, **310**, 181–213, doi:10.1017/S0022112096001772.
- Birkemeier, W. A., and C. Mason, 1984: The CRAB: A unique nearshore surveying vehicle. *J. Surv. Eng.*, **110**, 1–7, doi:10.1061/(ASCE)0733-9453(1984)110:1(1).

- Bowen, A. J., and R. T. Guza, 1978: Edge waves and surf beat. *J. Geophys. Res.*, **83**, 1913–1920, doi:[10.1029/JC083iC04p01913](https://doi.org/10.1029/JC083iC04p01913).
- , and R. A. Holman, 1989: Shear instabilities of the mean longshore current: 1. Theory. *J. Geophys. Res.*, **94**, 18 023–18 030, doi:[10.1029/JC094iC12p18023](https://doi.org/10.1029/JC094iC12p18023).
- Clark, D. B., S. Elgar, and B. Raubenheimer, 2012: Vorticity generation by short-crested wave breaking. *Geophys. Res. Lett.*, **39**, L24604, doi:[10.1029/2012GL054034](https://doi.org/10.1029/2012GL054034).
- Dodd, N., and E. B. Thornton, 1990: Growth and energetics of shear waves in the nearshore. *J. Geophys. Res.*, **95**, 16 075–16 083, doi:[10.1029/JC095iC09p16075](https://doi.org/10.1029/JC095iC09p16075).
- Eckart, C., 1951: Surface waves on water of variable depth. Scripps Institute of Oceanography Wave Rep. 100, SIO Reference 51-12, 60 pp.
- Elgar, S., and R. T. Guza, 1985: Observations of bispectra of shoaling surface gravity waves. *J. Fluid Mech.*, **161**, 425–448, doi:[10.1017/S0022112085003007](https://doi.org/10.1017/S0022112085003007).
- Feddersen, F., 2014: The generation of surfzone eddies in a strong alongshore current. *J. Phys. Oceanogr.*, **44**, 600–617, doi:[10.1175/JPO-D-13-051.1](https://doi.org/10.1175/JPO-D-13-051.1).
- , R. T. Guza, S. Elgar, and T. H. C. Herbers, 1996: Cross-shore structure of longshore currents during Duck94. *Proc. 25th Int. Conf. Coastal Engineering*, Orlando, FL, American Society of Civil Engineers, 3666–3679.
- , —, —, and —, 1998: Alongshore momentum balances in the nearshore. *J. Geophys. Res.*, **103**, 15 667–15 676, doi:[10.1029/98JC01270](https://doi.org/10.1029/98JC01270).
- Gallagher, E. L., S. Elgar, and R. T. Guza, 1998: Observations of sand bar evolution on a natural beach. *J. Geophys. Res.*, **103**, 3203–3215, doi:[10.1029/97JC02765](https://doi.org/10.1029/97JC02765).
- Garcez Faria, A. F., E. B. Thornton, T. P. Stanton, C. V. Soares, and T. C. Lippmann, 1998: Vertical profiles of longshore currents and related bed shear stress and bottom roughness. *J. Geophys. Res.*, **103**, 3217–3232, doi:[10.1029/97JC02265](https://doi.org/10.1029/97JC02265).
- , —, T. C. Lippmann, and T. P. Stanton, 2000: Undertow over a barred beach. *J. Geophys. Res.*, **105**, 16 999–17 010, doi:[10.1029/2000JC900084](https://doi.org/10.1029/2000JC900084).
- Geiman, J. D., and J. T. Kirby, 2013: Unforced oscillation of rip-current vortex cells. *J. Phys. Oceanogr.*, **43**, 477–497, doi:[10.1175/JPO-D-11-0164.1](https://doi.org/10.1175/JPO-D-11-0164.1).
- Gonella, J., 1972: A rotary-component method for analyzing meteorological and oceanographic vector time series. *Deep-Sea Res. Oceanogr. Abstr.*, **19**, 833–846, doi:[10.1016/0011-7471\(72\)90002-2](https://doi.org/10.1016/0011-7471(72)90002-2).
- Guza, R. T., and E. B. Thornton, 1980: Local and shoaled comparisons of sea surface elevations, pressures, and velocities. *J. Geophys. Res.*, **85**, 1524–1530, doi:[10.1029/JC085iC03p01524](https://doi.org/10.1029/JC085iC03p01524).
- , and —, 1985: Observations of surf beat. *J. Geophys. Res.*, **90**, 3161–3172, doi:[10.1029/JC090iC02p03161](https://doi.org/10.1029/JC090iC02p03161).
- Haines, J. W., and A. H. Sallenger Jr., 1994: Vertical structure of mean cross-shore currents across a barred surf zone. *J. Geophys. Res.*, **99**, 14 223–14 242, doi:[10.1029/94JC00427](https://doi.org/10.1029/94JC00427).
- Hannan, E. J., 1970: *Multiple Time Series*. Wiley, 536 pp.
- Howd, P. A., J. Oltman-Shay, and R. A. Holman, 1991: Wave variance partitioning in the trough of a barred beach. *J. Geophys. Res.*, **96**, 12 781–12 795, doi:[10.1029/91JC00434](https://doi.org/10.1029/91JC00434).
- Lippmann, T. C., and A. J. Bowen, 2016: The vertical structure of low-frequency motions in the nearshore. Part II: Theory. *J. Phys. Oceanogr.*, **46**, 3713–3727, doi:[10.1175/JPO-D-16-0015.1](https://doi.org/10.1175/JPO-D-16-0015.1).
- , R. A. Holman, and K. K. Hathaway, 1993: Episodic, non-stationary behavior of a double bar system at Duck, North Carolina, U.S.A., 1986–1991. *J. Coastal Res.*, **15**, 49–75. [Available online at <http://www.jstor.org/stable/25735723>.]
- , T. H. C. Herbers, and E. B. Thornton, 1999: Gravity and shear wave contributions to nearshore infragravity motions. *J. Phys. Oceanogr.*, **29**, 231–239, doi:[10.1175/1520-0485\(1999\)029<0231:GASWCT>2.0.CO;2](https://doi.org/10.1175/1520-0485(1999)029<0231:GASWCT>2.0.CO;2).
- Long, J. W., and H. T. Özkan-Haller, 2009: Low-frequency characteristics of wave group–forced vortices. *J. Phys. Oceanogr.*, **114**, C08004, doi:[10.1029/2008JC004894](https://doi.org/10.1029/2008JC004894).
- MacMahan, J. H., A. J. H. M. Reniers, E. B. Thornton, and T. P. Stanton, 2004a: Infragravity rip current pulsations. *J. Geophys. Res.*, **109**, C01033, doi:[10.1029/2003JC002068](https://doi.org/10.1029/2003JC002068).
- , —, —, and —, 2004b: Surf zone eddies coupled with rip current morphology. *J. Geophys. Res.*, **109**, C07004, doi:[10.1029/2003JC002083](https://doi.org/10.1029/2003JC002083).
- , —, and —, 2010: Vortical surf zone velocity fluctuations with O(10) min period. *J. Geophys. Res.*, **115**, C06007, doi:[10.1029/2009JC005383](https://doi.org/10.1029/2009JC005383).
- Newberger, P. A., and J. S. Allen, 2007: Forcing a three-dimensional, hydrostatic, primitive-equation model for application in the surf zone: 2. Application to DUCK94. *J. Geophys. Res.*, **112**, C08019, doi:[10.1029/2006JC003474](https://doi.org/10.1029/2006JC003474).
- Noyes, T. J., R. T. Guza, S. Elgar, and T. H. C. Herbers, 2004: Field observations of shear waves in the surf zone. *J. Geophys. Res.*, **109**, C01031, doi:[10.1029/2002JC001761](https://doi.org/10.1029/2002JC001761).
- Oltman-Shay, J., P. A. Howd, and W. A. Birkemeier, 1989: Shear instabilities of the mean longshore current: 2. Field data. *J. Geophys. Res.*, **94**, 18 031–18 042, doi:[10.1029/JC094iC12p18031](https://doi.org/10.1029/JC094iC12p18031).
- Ozkan-Haller, H. T., and J. T. Kirby, 1999: Nonlinear evolution of shear instabilities of the longshore current: A comparison of observations and computations. *J. Geophys. Res.*, **104**, 25 953–25 984, doi:[10.1029/1999JC900104](https://doi.org/10.1029/1999JC900104).
- Prandle, D., 1982: The vertical structure of tidal currents and other oscillatory flows. *Cont. Shelf Res.*, **1**, 191–207, doi:[10.1016/0278-4343\(82\)90004-8](https://doi.org/10.1016/0278-4343(82)90004-8).
- Priestley, M. B., 1981: *Spectral Analysis and Time Series*. Academic Press, 890 pp.
- Putrevu, U., and I. A. Svendsen, 1995: Infragravity velocity profiles in the surf zone. *J. Geophys. Res.*, **100**, 16 131–16 142, doi:[10.1029/95JC01284](https://doi.org/10.1029/95JC01284).
- , J. Oltman-Shay, and I. A. Svendsen, 1995: Effect of along-shore nonuniformities on longshore current predictions. *J. Geophys. Res.*, **100**, 16 119–16 130, doi:[10.1029/95JC01459](https://doi.org/10.1029/95JC01459).
- Reniers, A. J. H. M., J. A. Roelvink, and E. B. Thornton, 2004a: Morphodynamic modeling of an embayed beach under wave group forcing. *J. Geophys. Res.*, **109**, C01030, doi:[10.1029/2002JC001586](https://doi.org/10.1029/2002JC001586).
- , E. B. Thornton, T. P. Stanton, and J. A. Roelvink, 2004b: Vertical flow structure during SandyDuck: Observations and modeling. *Coastal Eng.*, **51**, 237–260, doi:[10.1016/j.coastaleng.2004.02.001](https://doi.org/10.1016/j.coastaleng.2004.02.001).
- Simons, R. R., T. J. Grass, and M. Mansour-Tehrani, 1992: Bottom shear stresses in the boundary layers under waves and currents crossing at right angles. *Proc. 23rd Int. Conf. on Coastal Engineering*, Venice, Italy, American Society of Civil Engineers, 604–617.
- Slinn, E. N., J. S. Allen, P. A. Newberger, and R. A. Holman, 1998: Nonlinear shear instabilities of alongshore currents over barred beaches. *J. Geophys. Res.*, **103**, 18 357–18 379, doi:[10.1029/98JC01111](https://doi.org/10.1029/98JC01111).
- Soulsby, R. L., 1990: Tidal-current boundary layers. *The Sea*, B. Le Mahoute and D. M. Hanes, Eds., Ocean Engineering Science, Vol. 9, Wiley and Sons, 523–566.
- Svendsen, I. A., 1984: Mass flux and undertow in a surf zone. *Coastal Eng.*, **8**, 347–365, doi:[10.1016/0378-3839\(84\)90030-9](https://doi.org/10.1016/0378-3839(84)90030-9).

- , and U. Putrevu, 1994: Nearshore mixing and dispersion. *Proc. Roy. Soc. London*, **A445**, 561–576, doi:[10.1098/rspa.1994.0078](https://doi.org/10.1098/rspa.1994.0078).
- , K. Haas, and Q. Zhao, 2002: Quasi-3D nearshore circulation model SHORECIRC. Center for Applied Coastal Research Internal Rep. CACR-02-01, 65 pp. [Available online at [http://math.robertobernetti.com/pub/Main/ModelloDiTrasporto/shorecirc2\\_0.pdf](http://math.robertobernetti.com/pub/Main/ModelloDiTrasporto/shorecirc2_0.pdf).]
- Thornton, E. B., and C. S. Kim, 1993: Longshore current and wave height modulation at tidal frequency inside the surf zone. *J. Geophys. Res.*, **98**, 16 509–16 519, doi:[10.1029/93JC01440](https://doi.org/10.1029/93JC01440).
- , and T. P. Stanton, 1994: Pressure and velocity observations from a movable sled platform during Duck 94. U.S. Army Corps of Engineers Field Research Facility, accessed 1 September 2016. [Available online at <http://www.frf.usace.army.mil/dksrv/dk94dir.html>.]
- Van Dongeren, A., and I. A. Svendsen, 2000: Nonlinear and 3D effects in leaky infragravity waves. *Coastal Eng.*, **41**, 467–496, doi:[10.1016/S0378-3839\(00\)00041-7](https://doi.org/10.1016/S0378-3839(00)00041-7).
- Visser, P. J., 1986: Wave basin experiments on bottom friction due to current and waves. *Proc. 20th Conf. on Coastal Engineering*, Taipei, Taiwan, American Society of Civil Engineers, 807–821.
- Zhao, Q., I. A. Svendsen, and K. Haas, 2003: Three-dimensional effects in shear waves. *J. Geophys. Res.*, **108**, 3270, doi:[10.1029/2002JC001306](https://doi.org/10.1029/2002JC001306).